

1 **The Earth's core as a reservoir of water**

2 Yunguo Li¹, Lidunka Vočadlo¹, Tao Sun² and John P. Brodholt^{1,3}

3 ¹*Department of Earth Sciences, University College London, Gower Street, London WC1E 6BT,*
4 *United Kingdom*

5 ²*Key Laboratory of Computational Geodynamics, College of Earth and Planetary Sciences,*
6 *University of Chinese Academy of Sciences, Beijing 100049, China*

7 ³*Centre for Earth Evolution and Dynamics, University of Oslo, Oslo, Norway*

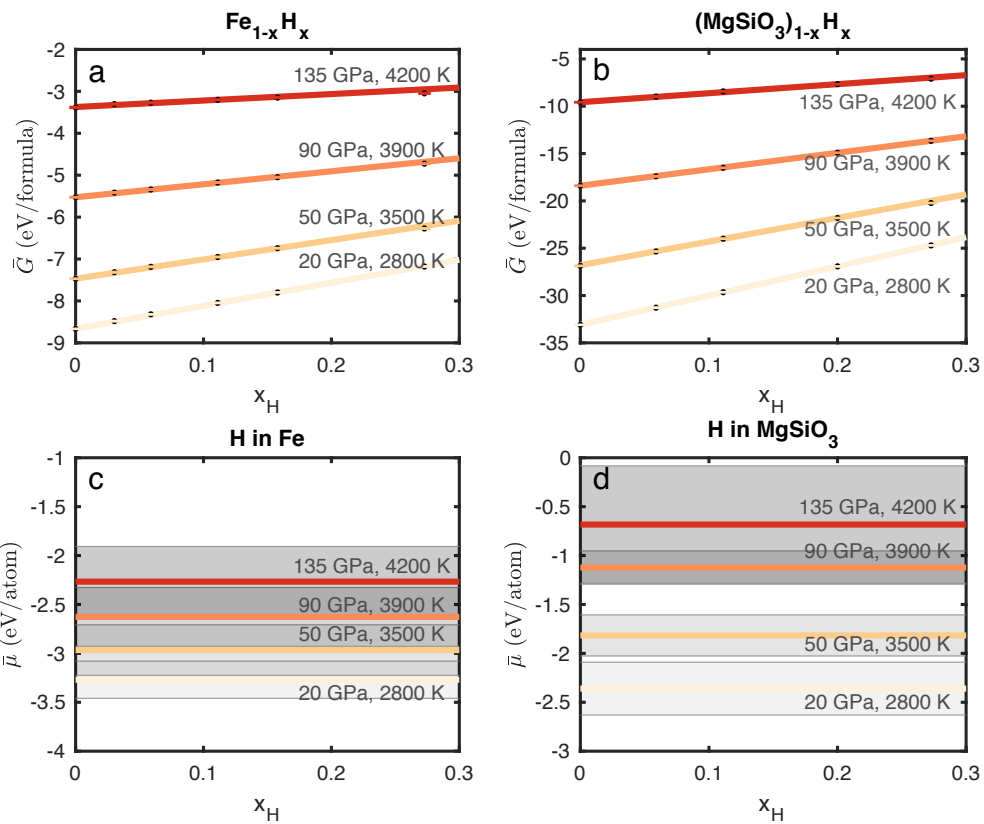
8
9 **Current estimates of the budget and distribution of water in the Earth have large**
10 **uncertainties, most of which come from the lack of information about the deep Earth. Recent**
11 **studies suggest that the Earth could have gained a considerable amount of water during the**
12 **early stages of Earth's evolution from the hydrogen-rich solar nebula, and that a large**
13 **amount of the water in the Earth may have partitioned into the core. Here, we calculate the**
14 **partitioning of water between iron and silicate melts at 20-135 gigapascals and 2800-5000**
15 **kelvin, using *ab initio* molecular dynamics and thermodynamic integration techniques. Our**
16 **results indicate a siderophile nature of water at core-mantle differentiation and core-mantle**
17 **boundary conditions, which can be weakened with increasing temperature; nevertheless, we**
18 **find that water always partitions strongly into the iron liquid at both reducing and oxidising**
19 **conditions. The siderophile nature of water is also verified by an empirical-counting method**
20 **showing the distribution of hydrogen in an equilibrated iron and silicate melt. We therefore**
21 **conclude that the Earth's core may act as a large reservoir containing most of the Earth's**
22 **water. In addition to constraining accretion models and water distribution, the findings may**
23 **partially account for the mismatch between mineral physics and seismic observations in the**
24 **Earth's core.**

26 Determining the water or hydrogen partition coefficient at high pressure (HP) high temperature
27 (HT) conditions between iron and silicate melts isn't easy due to the low scatter cross section area
28 of hydrogen, and therefore various methods have been used to detect hydrogen indirectly. In
29 1996, Kuramoto and Matsui¹ estimated the partition coefficient of hydrogen between iron and
30 silicate melts using a thermodynamic model based on gas solubility. They reported that hydrogen
31 is siderophile and the partitioning of hydrogen into iron increases with increasing pressure and
32 temperature. A year later, Okuchi² measured the hydrogen partition coefficient by calculating the
33 amount of hydrogen trapped in the bubbles of quenched FeH_x phases and determined the hydrogen
34 concentration in the silicate melt through mass balance calculations. Their result agreed with the
35 thermodynamic model in that over 95% of water accreted to the Earth should have reacted with
36 iron and gone into the core. Several years later, Shibazaki *et al.*³ employed a different method to
37 determine the hydrogen partition coefficient between solid iron and ringwoodite, for which they
38 estimated the hydrogen concentration in iron from hydrogenation-induced lattice expansion, and
39 by Fourier transform infrared spectroscopy (FTIR) in ringwoodite. Their experiments also indicate
40 a siderophile nature of hydrogen. In contrast, Zhang and Yin⁴ reported an almost neutral behavior
41 of hydrogen between liquid iron and silicate melts at 3200 K and 40 GPa by performing two-phase
42 *ab initio* molecular dynamics (AIMD) simulations. Recently, Clesi *et al.*⁵ used elastic recoil
43 detection analysis (ERDA) to determine hydrogen concentration in both iron and silicate melts at
44 pressures of 5~20 GPa. They obtained a hydrogen metal-silicate partition coefficient of ~0.2,
45 indicating lithophile behaviour of hydrogen. The contradiction to previous results was attributed
46 to fugacity and possibly also the presence of carbon in samples. Malavergne *et al.*⁶ coupled the use
47 of ERDA and Secondary Ion Mass Spectrometry (SIMS) to measure the hydrogen partition

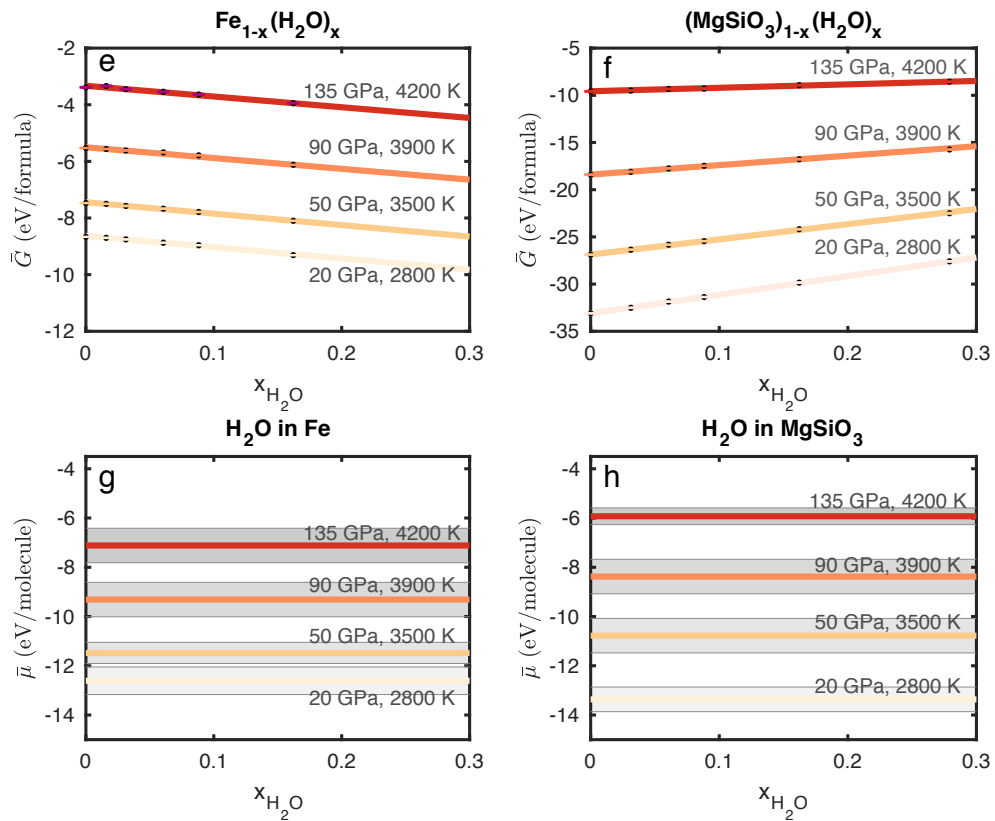
48 coefficient. Their study confirmed the pressure effect on hydrogen partitioning observed before,
49 and also suggest that hydrogen could change from lithophile to siderophile above ~15 GPa.

50 **Free energy calculations**

51 The discrepancies in the literature and the complexity of hydrogen partitioning hinder our further
52 understanding of water in the Earth and necessitate a comprehensive study that can accurately
53 describe the partitioning behaviour under various pressure, temperature and fugacity conditions.
54 *Ab initio* thermodynamics is a reliable and widely used method for partition calculations under
55 HP-HT conditions⁷. In this study, we have calculated the Gibbs free energy of a series of iron and
56 silicate melts with different concentrations of H₂/H₂O (see **Extended Data Table 1**) by performing
57 AIMD with thermodynamic integration. We considered two end-member systems: $P_{\text{H}_2\text{O}}/$
58 $P_{\text{H}_2+\text{H}_2\text{O}} = 1$ and $P_{\text{H}_2}/P_{\text{H}_2+\text{H}_2\text{O}} = 1$ (namely, in the context of experiments, iron and silicate are
59 equilibrated in the environment of pure H₂O or H₂ in these two cases), representing oxidised and
60 reduced conditions, respectively. The calculations were done at conditions above the solidus of
61 our silicate melt at 20, 50, 90 and 135 GPa⁸, corresponding to temperatures of 2800, 3500, 3900
62 and 4200 K, respectively. We express the Gibbs free energy by $G(p, T, x) = \bar{G}(p, T, x) - TS_{mix}$,
63 where x is the concentration of H or H₂O in iron or silicate melts, \bar{G} is the pure component of Gibbs
64 free energy, and the second term TS_{mix} is the entropy contribution from mixing. From calculated
65 Gibbs free energies, we derived the chemical potential of H/H₂O as $\mu_{\text{H}/\text{H}_2\text{O}}(p, T, x) =$
66 $\bar{\mu}_{\text{H}/\text{H}_2\text{O}}(p, T, x) - TS_{mix}^{\text{H}/\text{H}_2\text{O}}$ (see **Methods**). With the calculated chemical potentials
67 $\mu_{\text{H}/\text{H}_2\text{O}}(p, T, x)$, the partition coefficients can be derived. Here, we use “hydrogen” to refer to the
68 general definition of “water”, and use H₂ and H₂O to denote the hydrogen and water molecules,
69 respectively.



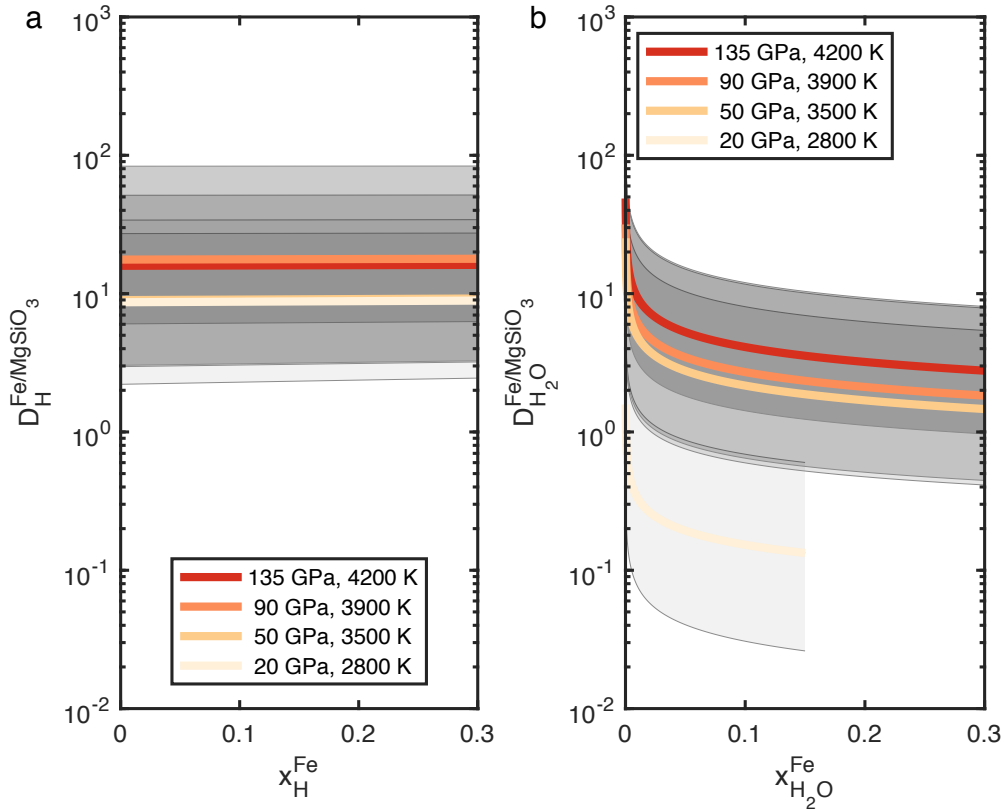
70



71

72 Figure 1: **Calculated free energies.** **a, b, e and f)** Calculated Gibbs free energies $\bar{G}(p, T, x)$ (points)
73 and their fits (curves) for $\text{Fe}_{1-x}\text{H}_x$, $(\text{MgSiO}_3)_{1-x}\text{H}_x$, $\text{Fe}_{1-x}(\text{H}_2\text{O})_x$ and $(\text{MgSiO}_3)_{1-x}(\text{H}_2\text{O})_x$ melts,
74 respectively. **c, d, g and h)** Derived $\bar{\mu}_{\text{H}/\text{H}_2\text{O}}(p, T, x)$ quantities in iron and silicate melts. Shaded
75 regions indicate uncertainties. See **Extended Data Table 1** for the raw data and **Supplementary**
76 **Information** for a better view with uncertainties.

77 **Fig. 1a and b** show our calculated Gibbs free energies $\bar{G}(p, T, x)$ of iron and silicate melts as a
78 function of hydrogen concentration, and **Fig. 1c and d** plot the derived $\bar{\mu}_{\text{H}}$. **Fig. 1e-h** show the
79 Gibbs free energies $\bar{G}(p, T, x)$ of iron and silicate melts with H_2O and the derived pure component
80 of chemical potential $\bar{\mu}_{\text{H}_2\text{O}}$. Under the same pressure, $\bar{\mu}_{\text{H}}$ is always lower in iron than in silicate.
81 This is indicative that H is siderophile. Similarly, $\bar{\mu}_{\text{H}_2\text{O}}$ in liquid iron is also lower than in silicate
82 melt from 50 to 135 GPa in **Fig. 1g and h**, suggesting a siderophile behavior of H_2O . While at 20
83 GPa, $\bar{\mu}_{\text{H}_2\text{O}}$ is slightly higher in liquid iron. This shows a pressure effect on H_2O partitioning.



84

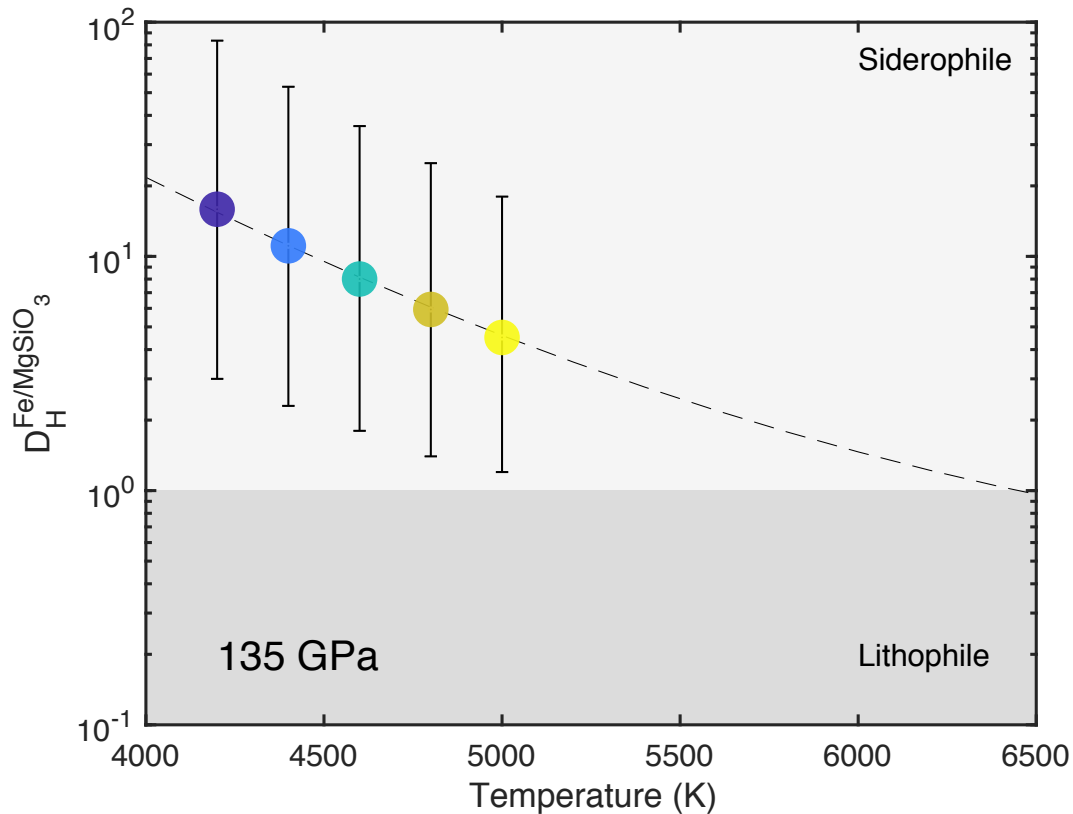
85 **Figure 2: Partition coefficient.** Derived partition coefficient between the iron and silicate melts
 86 as a function of concentration in iron for **a)** H and **b)** H₂O. Shaded regions are uncertainties. See
 87 **Supplementary Information** for a better view with uncertainties.

88 **Partitioning coefficients**

89 With the obtained free energies, we calculated the partition coefficient of H between iron and
 90 silicate melts (denoted by $D_H^{\text{Fe/MgSiO}_3}$) by equating the chemical potentials of H ($\mu_H(p, T, x)$) in
 91 both iron and silicate. As can be seen in **Fig. 2a**, $D_H^{\text{Fe/MgSiO}_3}$ does not show a visible dependence
 92 on x_H^{Fe} . $D_H^{\text{Fe/MgSiO}_3}$ is over 1 for all the examined pressures and compositions, showing a
 93 siderophile nature of H. The calculated partition coefficient of H₂O between iron and silicate melts
 94 $D_{\text{H}_2\text{O}}^{\text{Fe/MgSiO}_3}$ is shown in **Fig. 2b**. Generally speaking, H₂O is also siderophile except for at 20 GPa

95 where H₂O is slightly lithophile. $D_{\text{H}_2\text{O}}^{\text{Fe/MgSiO}_3}$ shows a sharp increase approaching the concentration
96 limit of $x_{\text{H}_2\text{O}}^{\text{Fe}}$, and such a behaviour is due to the entropy difference.

97 We did not include FeO in silicate melts nor O in the metal. The MgSiO₃ silicate is a good
98 approximation to the lower mantle⁹. According to the estimated O budget in the outer core and
99 FeO partition calculations¹⁰, the content of FeO in liquid MgSiO₃ should not be significant.
100 Furthermore, H atoms mainly pair with Fe and do not prefer an O-H bonding in liquid iron (see
101 **Supplementary Information**). Therefore, the presence of FeO in equilibrated iron and silicate
102 melts will have negligible effects on the siderophile character of hydrogen. The presence of ferric
103 iron in the silicate melt has also not been considered as the amount of ferric iron present during
104 core formation is likely to be very small¹¹. But regardless, the presence of ferric Fe₂O₃ should not
105 also change the siderophile behaviour of hydrogen as Fe₂O₃ in the silicate melt would be subjected
106 to the reaction: $\text{Fe}_2\text{O}_3 + 2\text{H} = 2\text{FeO} + \text{H}_2\text{O}$, and this transformation (H to H₂O) basically does not
107 change the siderophile nature of hydrogen.



108

109 **Figure 3: Temperature dependence of H partitioning.** Calculated partition coefficient

110 $D_H^{\text{Fe/MgSiO}_3}$ between iron and silicate melts as a function of temperature at 135 GPa. $D_H^{\text{Fe/MgSiO}_3}$

111 has little dependency on hydrogen concentration.

112 We have also explored the temperature dependence of H partitioning at 135 GPa – conditions

113 appropriate to the core-mantle boundary (CMB) today. Gibbs free energies at temperatures from

114 4200 to 5000 K were obtained by integrating the Gibbs–Helmholtz equation based on the

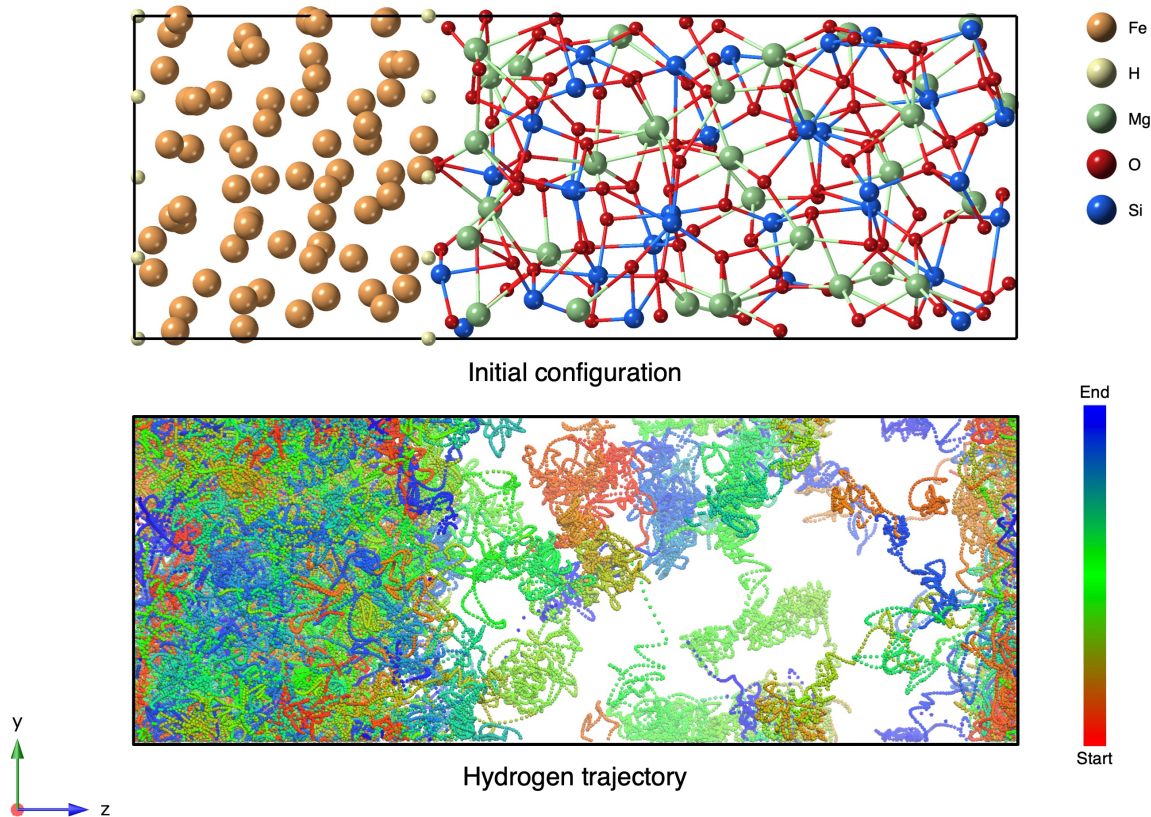
115 calculated temperature-dependent enthalpies (see **Extended Data Table 2**) and assuming the same

116 concentration dependence of Gibbs free energy to 4200 K. As shown in **Fig. 3**, $D_H^{\text{Fe/MgSiO}_3}$

117 decreases with increasing temperature and is significantly lowered over the range from 4200 to

118 5000 K. By extrapolating our data, we found that the temperature would need to reach over ~6500

119 K for H to become lithophile.

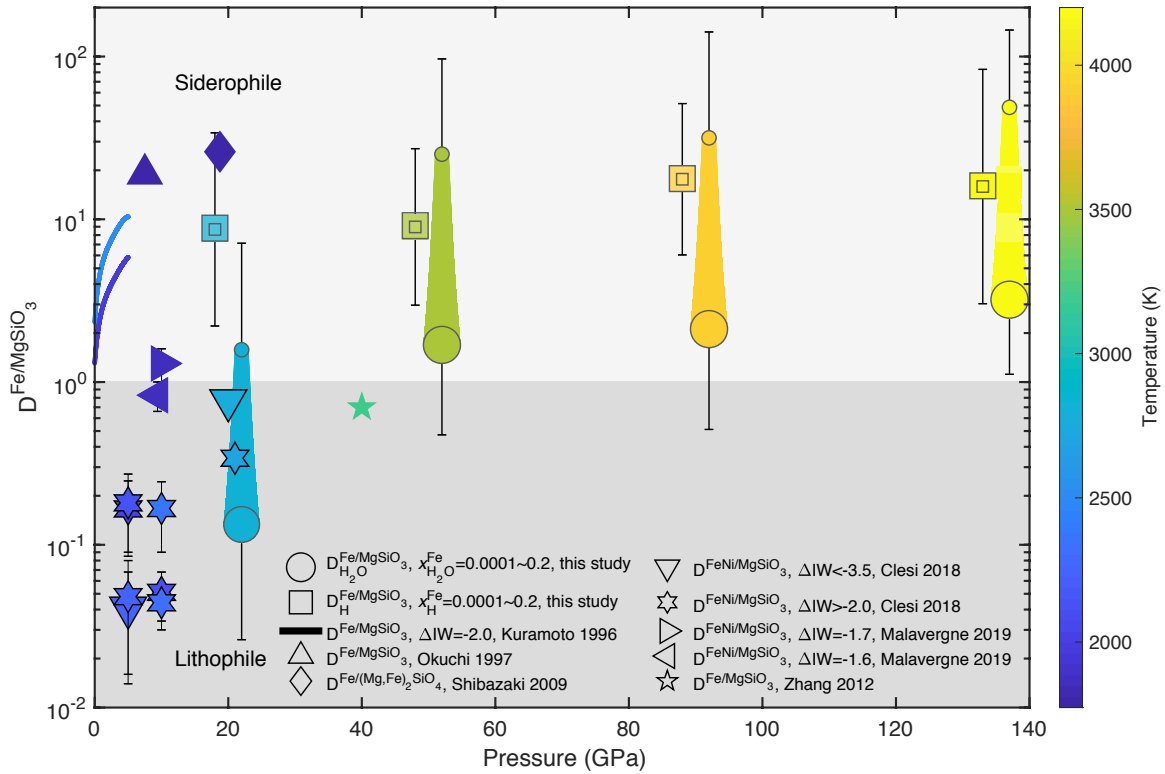


120

121 Figure 4: **Empirical counting of H partitioning**. Top panel: initial configuration of 12 hydrogen
 122 atoms sandwiched by 64 iron atoms and 32 formulas of MgSiO_3 for a NVT run of 10 *ps* at ~ 50
 123 GPa and 3500 K. Both iron and silicate are in melt state during the calculation. Bottom panel: Plot
 124 of the trajectories of the 12 hydrogen atoms.

125 In addition to the free energy calculations, we performed another calculation using the
 126 empirical-counting strategy to verify the findings above (see **Methods**). We built one supercell
 127 that contains a melt of 64 Fe atoms, a melt of 32 formula of MgSiO_3 and 12 H atoms sandwiched
 128 between the two melts; the system size was chosen to minimise surface area while maintaining
 129 computational efficiency. The calculation was run at ~ 50 GPa and 3500 K for 10 *ps*. **Fig. 4** shows
 130 the initial setting and AIMD trajectories (also see the **Supplementary Information** for the Movie).
 131 It can be seen that H atoms mostly reside in the Fe side during the run, showing the siderophile

132 nature of H. We counted the average number of H atoms at each side and obtained $D_{\text{H}}^{\text{Fe/MgSiO}_3} =$
133 3.1 ± 0.3 , which is lower than our free energy calculation result that gives $D_{\text{H}}^{\text{Fe/MgSiO}_3} = 9.1_{-6}^{+18}$.
134 It should be noted, however, that H diffuses much slower in silicate melt than in iron, so we might
135 overcount the residence chance of H in silicate and obtain a $D_{\text{H}}^{\text{Fe/MgSiO}_3}$ smaller than its true value.
136 The data from empirical counting may be improved with a longer run, bigger supercells
137 and multiple independent simulations. As well as H, some Si and O atoms also entered the iron
138 region which might also act to provide a slightly different $D_{\text{H}}^{\text{Fe/MgSiO}_3}$ compared to the free energy
139 calculations. Nevertheless, these simulations agree qualitatively with the free energy results. It
140 should be pointed out that Zhang and Yin⁴ obtained $D_{\text{H}}^{\text{Fe/MgSiO}_3} = 0.7 \pm 0.1$ using a similar two-
141 phase model at 40 GPa and 3200 K, which is lower than our value. The discrepancy is likely from
142 the setting of the two-phase model. They used a 44 iron atom cluster surrounded by silicate melt.
143 Such a small cluster has a large surface-to-volume ratio and a significant fraction of interface atoms,
144 and so probably does not represent the true partitioning between the bulk phases.



145

146 Figure 5: **Comparison of partition coefficients with the literature.** Compiled literature data in
 147 comparison with our partition coefficients of H and H₂O between iron and silicate melts calculated
 148 at 20, 50, 90 and 135 GPa, corresponding to 2800, 3500, 3900 and 4200 K. The partition
 149 coefficients of H and H₂O from this study were slightly shifted to lower and higher pressures,
 150 respectively, to facilitate a better view. The small and big squares (circles) indicate the partition
 151 coefficients of H (H₂O) at $x_{\text{H}/\text{H}_2\text{O}}^{\text{Fe}}=0.0001$ and 0.2, respectively.

152 Pressure and temperature dependence of water partitioning

153 In **Fig. 5**, we plot our partitioning coefficients of H and H₂O to compare with the literature. Our
 154 results agree with the findings of Kuramoto and Matsui¹, Okuchi² and Shibazaki *et al.*³, who
 155 determined the H concentration in iron via indirect methods. In contrast, Clesi *et al.*⁵ and
 156 Malavergne *et al.*⁶ found a more lithophile behaviour of hydrogen via direct methods. We note
 157 that H concentration is high in Okuchi's² experiments ($x_{\text{H}}^{\text{Fe}}>0.4$) and experiments of Shibazaki *et*

158 *al.*³ ($x_{\text{H}}^{\text{Fe}} > 0.5$), and is low in experiments of Clesi *et al.*⁵ and Malavergne *et al.*⁶ ($x_{\text{H}}^{\text{Fe}} < 0.03$). Our
159 results show that H is always siderophile at all possible ranges, and the difference between
160 experiments cannot be explained by the concentration difference. Experiments on the Fe-H system
161 show that hydrogen is nearly insoluble in both solid and liquid iron below 1 GPa^{12,13}, which
162 suggests that the hydrogen originally partitioned into iron at high pressure may have escaped upon
163 depressurisation, resulting in low concentrations in the Fe melt phase. In addition, Okuchi² found
164 that there is a minimum H₂O/MgSiO₃ molar ratio ($m \geq 1.0$) needed to keep P_{H_2} in the experiment
165 capsules, and in his experiments he used brucite, silicic acid and liquid H₂O to introduce hydrogen
166 in the system. While, in the experiments of Clesi *et al.*⁵ and Malavergne *et al.*⁶, hydrogen was
167 introduced into the system by adding Al(OH)₃ and brucite, and the H₂O/MgSiO₃ molar ratio is far
168 less than that in Okuchi's experiments². It is speculated that P_{H_2} is low in experiments of Clesi *et*
169 *al.*⁵ and Malavergne *et al.*⁶, and the actual condition could be more like our oxidising case
170 $P_{\text{H}_2\text{O}}/P_{\text{H}_2+\text{H}_2\text{O}} = 1$. Their partition coefficients also match ours at oxidising conditions.

171 Our H₂O partitioning coefficient strongly increases from 20 GPa to 50 GPa. The data of Clesi
172 *et al.*⁵ and Malavergne *et al.*⁶ at more oxidising conditions also show a similar trend from low
173 pressures to ~20 GPa. Unfortunately, their data do not extend to 50 GPa and so cannot be used to
174 confirm our high-pressure results, but the overlap at 20 GPa between our results and the
175 experimental results is reassuring. As for the temperature effect, Kuramoto and Matsui's¹ result
176 suggests that the increase of temperature strengthens the siderophile behaviour of H by using
177 extrapolated temperature-dependent molar volumes and solubilities in their thermodynamic model.
178 However, our free energy calculations clearly show the weakening of siderophile behaviour with
179 increasing temperature. We ran another empirical-counting simulation at ~50 GPa and 4000 K and
180 obtained $D_{\text{H}}^{\text{Fe}/\text{MgSiO}_3} = 2.1 \pm 0.3$, lower than that at ~50 GPa and 3500 K. This confirms that

181 $D_{\text{H}}^{\text{Fe/MgSiO}_3}$ decreases with increasing temperature. Apart from the pressure and temperature effects,
182 there is a strong difference in the absolute value of hydrogen partitioning depending on whether it
183 is H_2 or H_2O ; nevertheless, both species show siderophile behavior at high pressures relevant to
184 the core-mantle differentiation (CMD) and CMB conditions.

185 **Water in the deep Earth**

186 The calculated hydrogen partition coefficients imply that the Earth's core can potentially act as
187 a large reservoir of water. How much water is in the core depends on the amount of water dissolved
188 in the silicate melt during core-formation, which is related to the Earth accretion process, the CMD
189 process and the extent of equilibrium. If we assume a homogeneous accretion model of water to
190 the Earth and a single-stage core-forming process at 50 GPa and 3500 K, over 76% of hydrogen
191 will be partitioned into the core either at reducing conditions ($P_{\text{H}_2}/P_{\text{H}_2+\text{H}_2\text{O}}=1$) or under oxidising
192 conditions ($P_{\text{H}_2\text{O}}/P_{\text{H}_2+\text{H}_2\text{O}}=1$). This means that if the one ocean of water we see at the Earth's
193 surface was degassed from the mantle during or just after core-formation, then the core should
194 contain a minimum of five oceans of water. Alternatively, in the case of a late veneer scenario, the
195 Earth is almost free of water during the differentiation process and there would hardly be any water
196 in the core.

197 Interestingly, our results show that at current CMB conditions, H_2 and H_2O are both more
198 compatible in the core than in silicate melts. This means that any water held in a long lived deep
199 basal magma ocean¹⁴ would tend to partition strongly into the core, suggesting that deep mantle
200 anomalies resulting from a basal magma ocean (such as ULVZs and LLSVPs) should be relatively
201 dry. In addition, any water added to the deepest mantle via subduction will also have a tendency
202 to partition into the core now, either directly entering the core or reacting with liquid iron to form

203 iron oxide and release H₂ into the core¹⁵. Regardless of which or any of these processes are
204 occurring, the chemistry of the core should be subject to a constant change.

205 A recent model to explain the low D/H ratio of the Earth suggests a combination of chondritic
206 water and ingassing of nebular hydrogen, with four to five oceans of water are sequestered into
207 the core¹⁶. This was based on high hydrogen solubility at high pressures and mantle hydrogen
208 isotope fractionation. Our results are consistent with this model in that the core can be a reservoir
209 of water. Recent noble gas isotope studies¹⁷⁻¹⁹ and early-Earth ingassing modelling²⁰ also provide
210 strong evidence for the capture of nebular hydrogen during Earth' accretion. According to our
211 partitioning results, the core at present, therefore, could hold a significant amount of water.

212 The presence of abundant hydrogen in the core may change its seismic, electric and thermal
213 properties. Currently, core composition is still debated with an unexplained density deficit and low
214 seismic velocities²¹⁻²³. Umemoto and Hirose²⁴ show that ~1 wt.% H in the outer core can match
215 the compressional sound velocity and density, and suggest that hydrogen could be a primary light
216 element in the core. A core with 1 wt% hydrogen is equivalent to the hydrogen content of ~130
217 oceans of water. Even with our highest partition coefficients at 50 GPa and 3500 K, a core with
218 that much water would result in a mantle content of some 23 oceans of water. With one ocean at
219 the surface now, this implies that the current mantle should have 22 oceans of water, which is
220 above even the most optimistic saturation limits for the mantle²⁵, unless bridgmanite is able to
221 incorporate far more water than is currently expected²⁶. Furthermore, hydrogen should also be able
222 to partition into solid iron since the local environment of H in both solid and liquid iron is very
223 similar, and the possibility of H in the inner core may also improve our current understanding
224 about the inner core²⁷, for which only the multiple light elements model with carbon can explain
225 its seismic properties²⁸.

226 **References**

- 227 1 Kuramoto, K. & Matsui, T. Partitioning of H and C between the mantle and core during
228 the core formation in the Earth: Its implications for the atmospheric evolution and redox
229 state of early mantle. *J. Geophys. Res. Planets* **101**, 14909-14932 (1996).
- 230 2 Okuchi, T. Hydrogen partitioning into molten iron at high pressure: Implications for
231 earth's core. *Science* **278**, 1781-1784 (1997).
- 232 3 Shibazaki, Y., Ohtani, E., Terasaki, H., Suzuki, A. & Funakoshi, K.-i. Hydrogen
233 partitioning between iron and ringwoodite: Implications for water transport into the
234 Martian core. *Earth Planet. Sci. Lett.* **287**, 463-470 (2009).
- 235 4 Zhang, Y. & Yin, Q.-Z. Carbon and other light element contents in the Earth's core based
236 on first-principles molecular dynamics. *Proc. Natl. Acad. Sci.* **109**, 19579-19583 (2012).
- 237 5 Clesi, V. *et al.* Low hydrogen contents in the cores of terrestrial planets. *Sci. Adv.* **4**, 4-10
238 (2018).
- 239 6 Malavergne, V. *et al.* Experimental constraints on the fate of H and C during planetary
240 core-mantle differentiation. Implications for the Earth. *Icarus* **321**, 473-485 (2019).
- 241 7 Alfè, D., de Wijs, G. A., Kresse, G. & Gillan, M. J. Recent developments in ab initio
242 thermodynamics. *Int. J. Quantum Chem.* **77**, 871-879 (2000).
- 243 8 Stixrude, L. & Karki, B. Structure and Freezing of MgSiO₃; Liquid in Earth's Lower
244 Mantle. *Science* **310**, 297 (2005).
- 245 9 Garnero, E. J., McNamara, A. K. & Shim, S.-H. Continent-sized anomalous zones with
246 low seismic velocity at the base of Earth's mantle. *Nat. Geosci.* **9**, 481-489 (2016).
- 247 10 Pozzo, M., Davies, C., Gubbins, D. & Alfè, D. FeO Content of Earth's Liquid Core.
248 *Physical Review X* **9**, 041018 (2019).

249 11 Kaminsky, F. V. *et al.* Oxidation potential in the Earth's lower mantle as recorded by
250 ferropericlase inclusions in diamond. *Earth Planet. Sci. Lett.* **417**, 49-56 (2015).

251 12 Fukai, Y., Mori, K. & Shinomiya, H. The phase diagram and superabundant vacancy
252 formation in Fe–H alloys under high hydrogen pressures. *J. Alloys Compd.* **348**, 105-109
253 (2003).

254 13 Fukai, Y. The iron–water reaction and the evolution of the Earth. *Nature* **308**, 174-175
255 (1984).

256 14 Labrosse, S., Hernlund, J. W. & Coltice, N. A crystallizing dense magma ocean at the
257 base of the Earth's mantle. *Nature* **450**, 866-869 (2007).

258 15 Hu, Q. *et al.* FeO₂ and FeOOH under deep lower-mantle conditions and Earth's oxygen–
259 hydrogen cycles. *Nature* **534**, 241 (2016).

260 16 Wu, J. *et al.* Origin of Earth's water: Chondritic inheritance plus nebular ingassing and
261 storage of hydrogen in the core. *J. Geophys. Res. Planets* **123**, 2691-2712 (2018).

262 17 Bouhifd, M. A., Jephcoat, A. P., Heber, V. S. & Kelley, S. P. Helium in Earth's early
263 core. *Nat. Geosci.* **6**, 982-986 (2013).

264 18 Mukhopadhyay, S. & Parai, R. Noble gases: a record of Earth's evolution and mantle
265 dynamics. *Annu. Rev. Earth Planet. Sci.* **47**, 389-419 (2019).

266 19 Williams, C. D. & Mukhopadhyay, S. Capture of nebular gases during Earth's accretion
267 is preserved in deep-mantle neon. *Nature* **565**, 78-81 (2019).

268 20 Olson, P. & Sharp, Z. D. Hydrogen and helium ingassing during terrestrial planet
269 accretion. *Earth Planet. Sci. Lett.* **498**, 418-426 (2018).

270 21 Tkalčić, H. & Pham, T. S. Shear properties of Earth's inner core constrained by a
271 detection of J waves in global correlation wavefield. *Science* **362**, 329-332 (2018).

272 22 Hirose, K. *et al.* Crystallization of silicon dioxide and compositional evolution of the
273 Earth's core. *Nature* **543**, 99-102 (2017).

274 23 Badro, J., Brodholt, J. P., Piet, H., Siebert, J. & Ryerson, F. J. Core formation and core
275 composition from coupled geochemical and geophysical constraints. *Proc. Natl. Acad.*
276 *Sci.* **112**, 12310-12314 (2015).

277 24 Umemoto, K. & Hirose, K. Liquid iron-hydrogen alloys at outer core conditions by first-
278 principles calculations. *Geophys. Res. Lett.* **42**, 7513-7520 (2015).

279 25 Nakagawa, T. & Iwamori, H. On the implications of the coupled evolution of the deep
280 planetary interior and the presence of surface ocean water in hydrous mantle convection.
281 *Comptes Rendus Geoscience* **351**, 197-208 (2019).

282 26 Hernández, E. R., Alfè, D. & Brodholt, J. The incorporation of water into lower-mantle
283 perovskites: A first-principles study. *Earth Planet. Sci. Lett.* **364**, 37-43 (2013).

284 27 Militzer, B., Tagawa, S., Hirose, K. & Wahl, S. M. in *AGU Fall Meeting* (San
285 Francisco, 2016).

286 28 Li, Y., Vočadlo, L. & Brodholt, J. The elastic properties of *hcp*-Fe alloys under the
287 conditions of the Earth's inner core. *Earth Planet. Sci. Lett.* **493**, 118-127 (2018).

288

289 **Methods**

290 **Chemical potential of H/H₂O**

291 The chemical potential of H/H₂O in iron/silicate melt, $\mu_{\text{H}/\text{H}_2\text{O}}$, is the partial molar Gibbs free energy of H or H₂O:

$$292 \mu_{\text{H}/\text{H}_2\text{O}}(p, T, x) = \left(\frac{\partial G}{\partial n_{\text{H}/\text{H}_2\text{O}}} \right)_{p, T, n_{\text{Fe}/\text{MgSiO}_3}} \quad (1)$$

293 which is the free energy change when adding H or H₂O to the melts with all other conditions unchanged. We express
294 the system Gibbs free energy by

$$295 G(p, T, x) = \bar{G}(p, T, x) - TS_{\text{mix}} \quad (2)$$

296 where S_{mix} is the ideal mixing entropy, and $\bar{G}(p, T, x)$ is the pure component free energy and equal to the sum of
297 pure component of chemical potentials $\sum_{i=1}^n x_i \bar{\mu}_i$. The chemical potential also has two contributions, namely, the
298 pure component and the mixing, and is written as

$$299 \mu(p, T, x) = \bar{\mu}(p, T, x) - TS_{\text{mix}} \quad (3)$$

300 We performed statistical tests on the calculated data $\bar{G}(p, T, x)$ per formula for the Fe_{1-x}H_x, (MgSiO₃)_{1-x}H_x, Fe₁₋
301 _x(H₂O)_x and (MgSiO₃)_{1-x}(H₂O)_x systems, and the tests justify a linear model — the use of higher order polynomials is
302 statistically invalid. Therefore, we fitted the calculated $\bar{G}(p, T, x)$ with

$$303 \bar{G}(p, T, x) = a + bx \quad (4)$$

304 where a and b are coefficients. We used a weighted fitting with the weight as $(\sum_{i=1}^n \sigma_{x_i})/\sigma_{x_1}$, where x_i is the i^{th}
305 concentration and σ is the uncertainty of \bar{G} . $\bar{\mu}(p, T, x)$ for H and H₂O can be directly obtained, namely^{10,29},

$$306 \bar{\mu}_{\text{H}/\text{H}_2\text{O}}(p, T, x) = \bar{G}(p, T, x) + (1 - x) \frac{\partial \bar{G}(p, T, x)}{\partial x} = a + b \quad (5)$$

307 The ideal mixing entropy for the Fe_{1-x}H_x, (MgSiO₃)_{1-x}H_x, Fe_{1-x}(H₂O)_x and (MgSiO₃)_{1-x}(H₂O)_x systems are

$$308 S_{\text{mix}}^{\text{Fe}_{1-x}\text{H}_x} = -k_B T (x \ln x + (1 - x) \ln(1 - x)) \quad (6.1)$$

$$309 S_{\text{mix}}^{(\text{MgSiO}_3)_{1-x}\text{H}_x} = -k_B T \left(x \ln \left(\frac{x}{5-4x} \right) + (1 - x) \left(2 \ln \left(\frac{1-x}{5-4x} \right) + 3 \ln \left(\frac{3-3x}{5-4x} \right) \right) \right) \quad (6.2)$$

$$310 S_{\text{mix}}^{\text{Fe}_{1-x}(\text{H}_2\text{O})_x} = -k_B T \left(x \left(2 \ln \left(\frac{2x}{1+2x} \right) + \ln \left(\frac{x}{1+2x} \right) \right) + (1 - x) \ln \left(\frac{1-x}{1+2x} \right) \right) \quad (6.3)$$

$$311 S_{\text{mix}}^{(\text{MgSiO}_3)_{1-x}(\text{H}_2\text{O})_x} = -k_B T \left(x \left(2 \ln \left(\frac{2x}{5-2x} \right) + \ln \left(\frac{3-2x}{5-2x} \right) \right) + (1 - x) \left(2 \ln \left(\frac{1-x}{5-2x} \right) + 3 \ln \left(\frac{3-2x}{5-2x} \right) \right) \right) \quad (6.4)$$

312 respectively. k_B is the Boltzmann constant. Similarly, S_{mix}^{H/H_2O} can be calculated as $S_{mix}^{system} + (1-x) \frac{\partial S_{mix}^{system}}{\partial x}$. In
 313 equilibrium between iron and silicate melts, the chemical potential $\mu_{H/H_2O}(p, T, x)$ in iron is equal to that in silicate
 314 melt

$$315 \quad \bar{\mu}_H^{Fe}(p, T, x) - T \left(S_{mix}^{Fe_{1-x}H_x} + (1-x) \frac{\partial S_{mix}^{Fe_{1-x}H_x}}{\partial x} \right) = \bar{\mu}_H^{MgSiO_3}(p, T, y) - T \left(S_{mix}^{(MgSiO_3)_{1-y}H_y} + (1-y) \frac{\partial S_{mix}^{(MgSiO_3)_{1-y}H_y}}{\partial y} \right) \quad (7.1)$$

$$317 \quad \bar{\mu}_{H_2O}^{Fe}(p, T, x) - T \left(S_{mix}^{Fe_{1-x}(H_2O)_x} + (1-x) \frac{\partial S_{mix}^{Fe_{1-x}(H_2O)_x}}{\partial x} \right) = \bar{\mu}_{H_2O}^{MgSiO_3}(p, T, y) - T \left(S_{mix}^{(MgSiO_3)_{1-y}(H_2O)_y} + (1-y) \frac{\partial S_{mix}^{(MgSiO_3)_{1-y}(H_2O)_y}}{\partial y} \right) \quad (7.2)$$

319 where y is the concentration of H/H₂O in silicate. At each x , we can obtain y and $D_{H/H_2O}^{Fe/MgSiO_3} = x/y$ by solving
 320 equations 7.1/7.2 analytically. Hence, the solute concentration in silicate $x_{H/H_2O}^{MgSiO_3}$ can be easily derived for each
 321 solute fraction in iron x_{H/H_2O}^{Fe} based on chemical potential functions, and the partition coefficient can also be
 322 determined.

323 ***Ab initio* molecular dynamics**

324 The Born–Oppenheimer AIMD calculations were performed with the density functional theory (DFT). The
 325 projector augmented wave (PAW) method^{30,31} implemented in the VASP code^{32,33} was employed to treat ion-
 326 electron interactions within the frozen-core approximation. Exchange-correlation effects were treated in the
 327 generalized gradient approximation (GGA) parameterised by Perdew, Burke and Ernzerhof³⁴. The Fermi–Dirac
 328 statistics were used to populate single particle orbitals. The plane-wave basis was generated with valence
 329 configurations of Fe- $3p^6 3d^7 4s^1$, Mg- $2p^6 3s^2$, Si- $3s^2 3p^2$, O- $2s^2 2p^4$, and H- $1s^1$. There is a high-to-low spin transition in
 330 liquid iron, but the density difference between magnetic calculation and non-magnetic calculation at 20 GPa and
 331 2000 K is no more than 0.9%³⁵, and magnetism mainly shifts the volume/pressure without bringing apparent
 332 structural changes³⁶. The change to the chemical potential of H/H₂O by including magnetism is no more than 16/82
 333 meV at 20 GPa. As discussed in the main text, the pressure effect on hydrogen partitioning is mainly due to the rapid
 334 increase of the hydrogen chemical potential in the silicate, which changes much slower in iron. Thus, including
 335 magnetism basically does not change our conclusions and all calculations were performed without spin polarisation.

336 We modeled the iron melt with a supercell of 64 Fe atoms obtained by melting *hcp*-Fe, and used a supercell
 337 containing 32 formulas of MgSiO₃ for the silicate melt obtained by melting perovskite. Then we added H₂ or H₂O
 338 into the supercells. The examined compositions can be seen in **Extended Data Table 1**. A plane-wave energy cutoff
 339 of 600 eV and 800 eV for the iron melts and silicate melts, respectively, was able to converge the energy within 1
 340 meV/atom and pressure within 0.15 GPa together with a 2 × 2 × 2 Monkhorst-Pack k-mesh. To save computer
 341 time, we first run the calculations using a single Gamma point and an energy cutoff of 400 eV and 600 eV for the
 342 iron and silicate melts, respectively. We then made corrections to 600 eV and 800 eV with a 2 × 2 × 2 Monkhorst-
 343 Pack k-mesh, respectively, by doing free energy perturbation and thermodynamic integration^{37,38}.

344 The iron and silicate melts were first relaxed at target pressures of 20, 50, 90 and 135 GPa, corresponding to
 345 temperatures of 2800, 3500, 3900 and 4200 K (roughly above the solidus of silicate melt⁸). The relaxation was done
 346 with constrained NPT (constant number of atoms N, pressure P and temperature T) calculations that maintained the
 347 cubic supercell. A time step of 1 fs was used for all NPT runs. NPT calculations were run for over 10 ps and the
 348 lattice parameters were extracted from the last eight picoseconds. When shifting to different P-T conditions, the melt
 349 structures were allowed to relax long enough as approaching the new PT condition step-by-step. These derived
 350 lattice parameters were then used for NVT (constant number of atoms N, volume V and temperature T) calculations,
 351 which normally last over several picoseconds; the first picoseconds were discarded for free energy calculations.

352 **Thermodynamic integration**

353 Gibbs free energy of melts was calculated by performing thermodynamic integration (TI) to the Weeks-Chandler-
 354 Andersen (WCA) gas system, which has established thermodynamics and no liquid-gas transition^{39,40}. The
 355 efficiency of this approach has been recently demonstrated in calculating the melting curve of elemental systems³⁷.
 356 In this study we extend this method to the free energy calculation of mixtures. The WCA system is a truncated
 357 repulsive Lennard-Jones (rLJ) system characterized by the energy parameter ε and length parameter σ , for which the
 358 potential ϕ_{WCA} is defined as

$$359 \quad \phi_{\text{WCA}}(r) = \begin{cases} 4\varepsilon \left[\left(\frac{\sigma}{r}\right)^{12} - \left(\frac{\sigma}{r}\right)^6 \right] + \varepsilon, & r \leq 2^{1/6}\sigma \\ 0, & r > 2^{1/6}\sigma \end{cases} \quad (8)$$

360 The potential during the transition from the *ab initio* system to the WCA system can be denoted as $\phi_\lambda = \phi_{\text{WCA}} +$
 361 $\lambda\phi$, where λ is the coupling parameter and ϕ is the electronic free energy from *ab initio* calculation. ϕ_λ smoothly
 362 shifts from the *ab initio* to the WCA potential as $\lambda \rightarrow 0$ when we set $2^{1/6}\sigma$ to be less than the minimal bond length

363 in the *ab initio* system. Gibbs free energy is calculated as $G = F(V) + P_0V$, where $F(V)$ is the Helmholtz free
364 energy and P_0 is the target pressure. $F(V)$ can be determined via TI as

$$365 \quad F(V) = F_{\text{WCA}} + \frac{1}{N} \int_0^1 \langle \phi_\lambda \rangle d\lambda = F_{\text{WCA}} + \frac{1}{Nm} \int_0^1 \frac{\langle \phi_\lambda \rangle}{\lambda^{m-1}} d\lambda^m \quad (9)$$

366 Where N is the number of atoms in the system and F_{WCA} is the documented free energy of the WCA gas^{39,40}. We
367 followed the previous study to transform λ to λ^m in order to ensure the integrand can be expressed in low-order
368 polynomials³⁷. A six-point Gaussian-Legendre quadrature was sufficient to converge the integral. F_{WCA} was
369 calculated by $F_{\text{WCA}} = F_{\text{ig}} + F'_{\text{WCA}}$, where F_{ig} is the ideal gas free energy and F'_{WCA} is the free energy difference
370 between the ideal gas and the WCA system, and

$$371 \quad F_{\text{ig}} = -k_B T \sum_{i=1}^n \ln Z_i = -k_B T \sum_{i=1}^n n \ln \left(\frac{\Omega}{N_i \Lambda_i^{3N_i}} \right) = k_B T \sum_{i=1}^n \left[n \ln \frac{\Lambda_i^3}{V} - 1 \right] \quad (10)$$

372 for the multicomponent system, where Ω is the system volume, V is the volume per atom, n is the number of
373 elements, and Z_i , N_i and Λ_i are the partition function, number of atoms and thermal wavelength for element i ,
374 respectively. $\Lambda_i = h/\sqrt{2\pi m_i k_B T}$, where h is the Planck constant, m_i is the mass of element i .

375 The uncertainties of $\langle \phi_\lambda \rangle$ were obtained by using blocking method and integrated to obtain the uncertainty of \bar{G} .
376 The uncertainties of $\bar{\mu}_{\text{H}/\text{H}_2\text{O}}$ were derived following the error propagation rule.

377 **Empirical-counting strategy**

378 At 50 GPa and 3500 K, we first relaxed both the iron (64 Fe atoms) and silicate (32 formulas of MgSiO_3) melt
379 structures into a rectangular supercell with a square x - y plane of $9 \times 9 \text{ \AA}^2$. Then, we combined the two supercells
380 into one with some space between the two parts in order to place 12 hydrogen atoms. Six hydrogen atoms were
381 inserted at each of the two Fe/ MgSiO_3 interfaces. The integrated supercell was equilibrated within NVT ensemble
382 for 10 ps at 3500 K. For each MD step, we calculated the bond length for every hydrogen atom, which was tagged as
383 a residence in the iron if its nearest neighbor atom is Fe apart from hydrogen. Finally, we obtained a partition
384 coefficient $D_{\text{H}}^{\text{Fe}/\text{MgSiO}_3} = 3.1 \pm 0.3$.

385 **Data availability**

386 The raw outputs can be accessed in the UK National Geoscience Data Centre (NGDC)
387 (<https://dx.doi.org/10.5285/d0677edf-c987-497d-aae8-23bf22ef774d>). Any additional data can
388 be requested by e-mailing the corresponding author.

389 **Code availability**

390 The Vienna *Ab Initio* Simulation Package (VASP) is a proprietary software available for
391 purchase at <https://www.vasp.at/>.

392 **References**

- 393 8 Stixrude, L. & Karki, B. Structure and Freezing of MgSiO₃; Liquid in Earth's Lower
394 Mantle. *Science* **310**, 297 (2005).
- 395 10 Pozzo, M., Davies, C., Gubbins, D. & Alfè, D. FeO Content of Earth's Liquid Core.
396 *Physical Review X* **9**, 041018 (2019).
- 397 29 Li, Y., Vočadlo, L., Alfè, D. & Brodholt, J. Carbon partitioning between the Earth's inner
398 and outer core. *J. Geophys. Res.:Solid Earth* **n/a**, doi:10.1029/2019JB018789 (2019).
- 399 30 Kresse, G. & Furthmüller, J. Efficiency of ab-initio total energy calculations for metals
400 and semiconductors using a plane-wave basis set. *Comput. Mater. Sci.* **6**, 15-50 (1996).
- 401 31 Kresse, G. & Hafner, J. *Ab initio* molecular dynamics for open-shell transition metals.
402 *Phys. Rev. B* **48**, 13115 (1993).
- 403 32 Kresse, G. & Joubert, D. From ultrasoft pseudopotentials to the projector augmented-
404 wave method. *Phys. Rev. B* **59**, 1758 (1999).
- 405 33 Blöchl, P. E. Projector augmented-wave method. *Phys. Rev. B* **50**, 17953 (1994).
- 406 34 Perdew, J. P., Burke, K. & Ernzerhof, M. Generalized gradient approximation made
407 simple. *Phys. Rev. Lett.* **77**, 3865-3868 (1996).
- 408 35 Edgington, A. L. *The Structure, Composition and Evolution of Mercury's Core* Ph.D
409 thesis, UCL (University College London), (2016).
- 410 36 Prescher, C. *et al.* Structurally hidden magnetic transitions in Fe₃C at high pressures.
411 *Phys. Rev. B* **85**, 140402-140402 (2012).

- 412 37 Sun, T., Brodholt, J. P., Li, Y. & Vočadlo, L. Melting properties from ab initio free
413 energy calculations: Iron at the Earth's inner-core boundary. *Phys. Rev. B* **98**, 224301-
414 224301 (2018).
- 415 38 Vočadlo, L. & Alfè, D. Ab initio melting curve of the fcc phase of aluminum. *Phys. Rev.*
416 *B* **65**, 1-12 (2002).
- 417 39 Bharadwaj, A. S. & Singh, Y. Fluid-solid transition in simple systems using density
418 functional theory. *J. Chem. Phys.* **143** (2015).
- 419 40 Mirzaeinia, A., Feyzi, F. & Hashemianzadeh, S. M. Equation of state and Helmholtz free
420 energy for the atomic system of the repulsive Lennard-Jones particles. *J. Chem. Phys.*
421 **147** (2017).

422

423 **Acknowledgements**

424 This work was supported by NERC grant NE/M015181/1 and NE/S01134X/1. We acknowledge
425 use of the NEXCS system, a collaborative facility supplied under the Joint Weather and Climate
426 Research Program, a strategic partnership between the Met Office and the Natural Environment
427 Research Council. This work also used the ARCHER UK National Supercomputing Service.
428 T.S. acknowledges the Strategic Priority Research Program (B) of the Chinese Academy of
429 Sciences (Grant No. XDB18000000). We finally thank the reviewers for valuable comments.

430 **Author Contributions**

431 Y.L. carried out the simulations and analysis. L.V. and J.B supervised the project. All authors
432 contributed to data analysis and writing the paper.

433 **Competing interests**

434 The authors declare no competing interests.

435 **Corresponding author**

436 Correspondence to Yunguo Li (email: Yunguo.li@ucl.ac.uk).

437

438 **Figure Captions**

439 **Figure 1: Calculated free energies.** **a, b, e and f)** Calculated Gibbs free energies $\bar{G}(p, T, x)$ (points)
440 and their fits (curves) for $\text{Fe}_{1-x}\text{H}_x$, $(\text{MgSiO}_3)_{1-x}\text{H}_x$, $\text{Fe}_{1-x}(\text{H}_2\text{O})_x$ and $(\text{MgSiO}_3)_{1-x}(\text{H}_2\text{O})_x$ melts,
441 respectively. **c, d, g and h)** Derived $\bar{\mu}_{\text{H}/\text{H}_2\text{O}}(p, T, x)$ quantities in iron and silicate melts. Shaded
442 regions indicate uncertainties. See **Extended Data Table 1** for the raw data and **Supplementary**
443 **Information** for a better view with uncertainties.

444 **Figure 2: Partition coefficient.** Derived partition coefficient between the iron and silicate melts
445 as a function of concentration in iron for **a)** H and **b)** H_2O . Shaded regions are uncertainties. See
446 **Supplementary Information** for a better view with uncertainties.

447 **Figure 3: Temperature dependence of H partitioning.** Calculated partition coefficient
448 $D_{\text{H}}^{\text{Fe}/\text{MgSiO}_3}$ between iron and silicate melts as a function of temperature at 135 GPa. $D_{\text{H}}^{\text{Fe}/\text{MgSiO}_3}$
449 has little dependency on hydrogen concentration.

450 **Figure 4: Empirical counting of H partitioning.** Top panel: initial configuration of 12 hydrogen
451 atoms sandwiched by 64 iron atoms and 32 formulas of MgSiO_3 for a NVT run of 10 ps at ~50
452 GPa and 3500 K. Both iron and silicate are in melt state during the calculation. Bottom panel: Plot
453 of the trajectories of the 12 hydrogen atoms.

454 **Figure 5: Comparison of partition coefficients with the literature.** Compiled literature data in
455 comparison with our partition coefficients of H and H_2O between iron and silicate melts calculated
456 at 20, 50, 90 and 135 GPa, corresponding to 2800, 3500, 3900 and 4200 K. The partition
457 coefficients of H and H_2O from this study were slightly shifted to lower and higher pressures,

458 respectively, to facilitate a better view. The small and big squares (circles) indicate the partition
 459 coefficients of H (H₂O) at $x_{\text{H}/\text{H}_2\text{O}}^{\text{Fe}}=0.0001$ and 0.2, respectively.

460
 461 **Extended Data Table 1 | Calculated free energies.** Calculated volumes and Gibbs free energies
 462 $\bar{G}(p, T, x)$ of iron and silicate melts with H and H₂O at 20, 50, 90, and 135 GPa, corresponding to
 463 temperatures of 2800, 3500, 3900 and 4200 K, respectively.

Material	P (GPa)	T (K)	V (Å ³ /atom)	\bar{G} (eV/atom)
Fe ₆₄	20	2800	10.798	-8.665±0.008
	50	3500	9.999	-7.472±0.009
	90	3900	9.148	-5.527±0.011
	135	4200	8.509	-3.385±0.016
Fe ₆₄ H ₂	20	2800	10.578	-8.481±0.011
	50	3500	9.751	-7.315±0.013
	90	3900	8.934	-5.416±0.014
	135	4200	8.312	-3.048±0.013
Fe ₆₄ H ₄	20	2800	10.372	-8.320±0.009
	50	3500	9.544	-7.186±0.011
	90	3900	8.756	-5.342±0.013
	135	4200	8.125	-3.270±0.017
Fe ₆₄ H ₈	20	2800	9.936	-8.047±0.010
	50	3500	9.132	-6.951±0.011
	90	3900	8.372	-5.175±0.013
	135	4200	7.766	-3.202±0.013
Fe ₆₄ H ₁₂	20	2800	9.557	-7.798±0.007
	50	3500	8.776	-6.742±0.011
	90	3900	8.045	-5.048±0.013
	135	4200	7.449	-3.150±0.014
Fe ₆₄ H ₂₄	20	2800	8.662	-7.178±0.008
	50	3500	7.913	-6.271±0.011
	90	3900	7.222	-4.726±0.011
	135	4200	6.687	-3.048±0.013
Fe ₆₂ (H ₂ O) ₁	20	2800	10.515	-8.240±0.008
	50	3500	9.693	-7.127±0.014
	90	3900	8.880	-5.284±0.012
	135	4200	8.245	-3.246±0.014
Fe ₆₂ (H ₂ O) ₂	20	2800	10.263	-8.240±0.008
	50	3500	9.429	-7.127±0.014
	90	3900	8.640	-5.284±0.012
	135	4200	8.031	-3.246±0.014
Fe ₆₂ (H ₂ O) ₄	20	2800	9.799	-7.912±0.007
	50	3500	8.986	-6.840±0.012
	90	3900	8.202	-5.067±0.012
	135	4200	7.618	-3.158±0.014
Fe ₆₂ (H ₂ O) ₆	20	2800	9.380	-7.618±0.008
	50	3500	8.604	-6.619±0.013
	90	3900	7.846	-4.919±0.012

	135	4200	7.263	-3.092±0.013
Fe ₆₂ (H ₂ O) ₁₂	20	2800	8.513	-7.032±0.008
	50	3500	7.744	-6.114±0.012
	90	3900	7.021	-4.621±0.010
	135	4200	6.484	-2.978±0.013
(MgSiO ₃) ₃₂	20	2800	9.984	-6.618±0.006
	50	3500	8.277	-5.373±0.008
	90	3900	7.281	-3.680±0.007
	135	4200	6.617	-1.915±0.008
(MgSiO ₃) ₃₂ H ₄	20	2800	9.763	-6.509±0.008
	50	3500	8.182	-5.267±0.008
	90	3900	7.199	-3.624±0.010
	135	4200	6.505	-1.850±0.010
(MgSiO ₃) ₃₂ H ₈	20	2800	9.639	-6.410±0.008
	50	3500	8.115	-5.191±0.009
	90	3900	7.089	-3.551±0.010
	135	4200	6.424	-1.826±0.010
(MgSiO ₃) ₃₂ H ₁₂	20	2800	9.522	-6.320±0.008
	50	3500	8.017	-5.174±0.009
	90	3900	6.986	-3.493±0.010
	135	4200	6.338	-1.814±0.010
(MgSiO ₃) ₃₂ H ₂₄	20	2800	9.272	-6.086±0.008
	50	3500	7.744	-4.900±0.009
	90	3900	6.743	-3.347±0.010
	135	4200	6.091	-1.783±0.010
(MgSiO ₃) ₃₁ (H ₂ O) ₁	20	2800	9.821	-6.584±0.008
	50	3500	8.210	-5.337±0.008
	90	3900	7.216	-3.667±0.011
	135	4200	6.539	-1.924±0.010
(MgSiO ₃) ₃₁ (H ₂ O) ₂	20	2800	9.758	-6.528±0.008
	50	3500	8.155	-5.293±0.008
	90	3900	7.154	-3.637±0.008
	135	4200	6.483	-1.911±0.010
(MgSiO ₃) ₃₁ (H ₂ O) ₃	20	2800	9.680	-6.503±0.007
	50	3500	8.072	-5.276±0.008
	90	3900	7.099	-3.621±0.008
	135	4200	6.437	-1.925±0.010
(MgSiO ₃) ₃₁ (H ₂ O) ₆	20	2800	9.416	-6.383±0.010
	50	3500	7.894	-5.173±0.008
	90	3900	6.931	-3.587±0.010
	135	4200	6.270	-1.910±0.010
(MgSiO ₃) ₃₁ (H ₂ O) ₁₂	20	2800	9.038	-6.212±0.010
	50	3500	7.570	-5.064±0.013
	90	3900	6.631	-3.543±0.010
	135	4200	6.002	-1.925±0.010
(MgSiO ₃) ₃₁ (H ₂ O) ₁₆	135	4200	5.841	-1.937±0.010

464

465 **Extended Data Table 2 | Temperature dependence of free energies.** Calculated volumes,

466 enthalpies and Gibbs free energies $\bar{G}(p, T, x)$ of Fe₆₄, Fe₆₄H₄, (MgSiO₃)₃₂ and (MgSiO₃)₃₂H₈ at

467 temperatures from 4200 to 5000 K under 135 GPa.

Material	T (K)	V ($\text{\AA}^3/\text{atom}$)	H (eV/atom)	\bar{G} (eV/atom)
Fe ₆₄	4200	8.509	1.150	-3.385
	4400	8.529	1.222	-3.603
	4600	8.568	1.313	-3.824
	4800	8.601	1.407	-4.050
	5000	8.627	1.497	-4.279
Fe ₆₄ H ₄	4200	8.125	1.052	-3.270
	4400	8.162	1.122	-3.477
	4600	8.197	1.209	-3.688
	4800	8.219	1.307	-3.903
	5000	8.249	1.387	-4.122
(MgSiO ₃) ₃₂	4200	6.617	0.600	-1.915
	4400	6.642	0.684	-2.037
	4600	6.677	0.754	-2.162
	4800	6.687	0.868	-2.291
	5000	6.716	0.943	-2.424
(MgSiO ₃) ₃₂ H ₈	4200	6.424	0.641	-1.826
	4400	6.453	0.730	-1.946
	4600	6.473	0.794	-2.069
	4800	6.511	0.909	-2.196
	5000	6.534	0.972	-2.326